nature electronics

Article

https://doi.org/10.1038/s41928-026-01613-4

Solid neon as a noise-resilient host for electron qubits above 100 mK

Received: 8 February 2025

Accepted: 18 March 2026

Published online: 29 April 2026

Check for updates

Xinhao Li[1,2], Christopher S. Wang[3], Brennan Dizdar[3], Yizhong Huang[1,4], Yutian Wen[5], Wei Guo[6,7], Xufeng Zhang[4], Xu Han[1,8] ✉, Xianjing Zhou[6,7] ✉ & Dafei Jin[1,5] ✉

Solid neon can be used as a solid host for single-electron qubits. At temperatures of around 10 mK, electron-on-solid-neon charge qubits exhibit long coherence times and high operation fidelities. However, a systematic characterization of the noise features of such systems is needed for the development of scalable quantum information architectures. Here we show that solid neon can be used as a noise-resilient host for electron qubits above 100 mK. We examine the resilience of solid neon against charge and thermal noise when electron-on-solid-neon charge qubits are operated away from the charge-insensitive sweet spot and at elevated temperatures. We show that the extracted high-frequency charge noise density of electron-on-solid-neon qubits, projected as voltage fluctuations on nearby electrodes, is between 10^{-4} μV^2 Hz^{-1} and 10^{-6} μV^2 Hz^{-1} at 0.01 MHz to 1 MHz, which is comparable to common semiconductor hosts. We also show that the electron-on-solid-neon charge qubits operating at frequencies of around 5 GHz can maintain echo coherence times of over 1 μs at temperatures up to 400 mK.

Solid-state electron qubits are subject to various decoherence channels from their host materials. Noise spectral analyses find a characteristic 1/*f* behaviour for electron charge or spin qubits, which is typically attributed to charge fluctuators in the bulk or at the interfaces of the host materials[1,2]. The coherence of electron qubits can be extended by reducing the noise density in their hosting environment and by minimizing their susceptibility to noise[2,3]. We recently showed that solid neon can be a host material that traps electrons at the vacuum/neon interface[4,5]. The charge states of electrons on solid neon can be addressed by coupling them with superconducting resonators in a circuit quantum electrodynamics architecture. At the charge sweet spot, they are first-order insensitive to charge noise and exhibit long coherence times T_2^* up to ~50 μs (ref. 5). This is nearly four orders of magnitude longer than that of semiconductor charge qubits[6]. The long coherence of electron-on-solid-neon (eNe) charge qubits also leads to long coherence eNe spin qubits[7–9].

However, eNe charge qubits are susceptible to environmental decoherence channels. Thus, understanding the performance of eNe qubits away from the sweet spot and at elevated temperatures, where they are subject to charge and thermal noise, is important for improving qubit uniformity, which is crucial for the generation and retention of entangled states[1]. Such studies are also required for the development of eNe spin qubits[7,9,10] through electrically sensitive mechanisms, such as exchange interactions[11–16] and synthetic spin–orbit coupling[17–21]. Furthermore, operating qubits at elevated temperatures can mitigate engineering constraints created due to the low cooling power at millikelvin temperatures and can aid the scaling up of the technology[22,23].

In this Article, we report the characterization of the noise features of solid neon. We use eNe qubits to probe the environmental noise on solid neon films by exploiting the increased charge sensitivity of the qubits when biased away from the sweet spots. We show that the

[1]Center for Nanoscale Materials, Argonne National Laboratory, Lemont, IL, USA. [2]Department of Physics, Harvard University, Cambridge, MA, USA. [3]James Franck Institute and Department of Physics, University of Chicago, Chicago, IL, USA. [4]Department of Electrical and Computer Engineering, Northeastern University, Boston, MA, USA. [5]Department of Physics and Astronomy, University of Notre Dame, Notre Dame, IN, USA. [6]National High Magnetic Field Laboratory, Tallahassee, FL, USA. [7]Department of Mechanical and Aerospace Engineering, FAMU-FSU College of Engineering, Florida State University, Tallahassee, FL, USA. [8]Pritzker School of Molecular Engineering, University of Chicago, Chicago, IL, USA. ✉e-mail: xu.han@anl.gov; xianjing.zhou@fsu.edu; dfjin@nd.edu

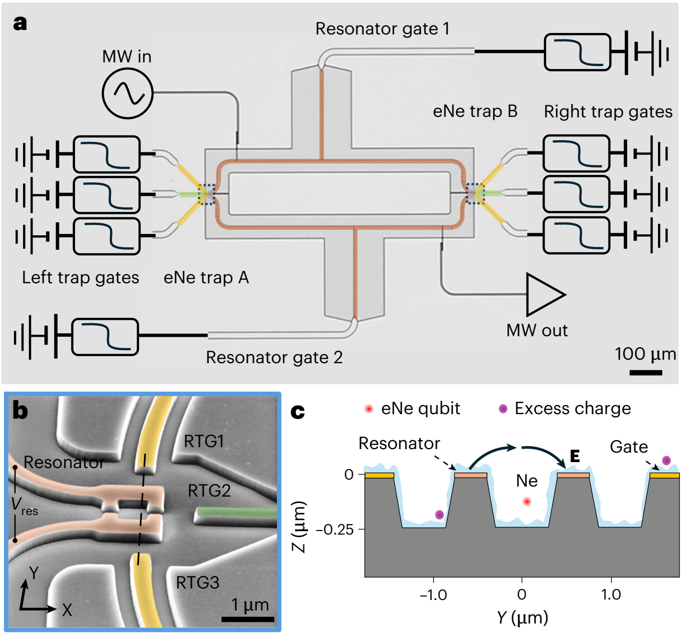

Fig. 1 | eNe charge qubit coupled to a TiN high-impedance superconducting resonator. a, Illustration of the high-impedance TiN superconducting resonator with two identical electron traps, MW input and output couplers, and d.c. gates. The metal plane between the resonator pins is connected to the ground plane via aluminium wire bonds. **b**, False-colour scanning electron micrograph image of the electron-trapping area on the right-hand side of the resonator with trap gates. A resonator bias voltage V_{res} was applied symmetrically to the two pins of the resonator via the resonator gates in **a**. **c**, Cross-section schematic of the electron-trapping area following the black dashed line in **b**. The charge state of eNe qubit is coupled with the MW electric field **E** within the resonator. RTG, resonator trap gate.

extracted high-frequency charge noise density of eNe, projected as voltage fluctuations on nearby electrodes, is between 10^{-4} μV^2 Hz^{-1} and 10^{-6} μV^2 Hz^{-1} at 0.01 MHz to 1 MHz. This is lower than that of some common semiconductor hosts[11–14,17–21,24–26] and approaches the best noise performance achieved on GaAs/AlGaAs platforms (10^{-6} μV^2 Hz^{-1} to 10^{-7} μV^2 Hz^{-1}; refs. 15,16). We also show variations in noise density and qubit properties, which could be attributed to disorders on solid neon films that trap excess electrons and open other decoherence channels. Furthermore, we show that eNe qubits operated near ~5 GHz can maintain echo coherence times exceeding 1 μs at temperatures of up to 400 mK, which are primarily limited by thermally increased energy relaxation and dephasing rates.

Device structure

Our device consists of a split superconducting resonator made from a 30-nm-thick titanium nitride (TiN) film grown on a ⟨111⟩-oriented intrinsic silicon substrate by atomic layer deposition[27] (Fig. 1a). An electron trap at each end of the resonator was surrounded by direct current (d.c.) gates, which were used to tune the qubit frequency, as shown in Fig. 1b. The differential mode of the resonator was coupled with the motional states of electrons trapped on the solid neon, with the microwave (MW) electrical field pointing from one resonator pin to the other, as shown in Fig. 1c. Considering the first two charge states of eNe, the coupled system can be described by the Jaynes–Cummings Hamiltonian[28]:

$$H = \hbar\omega_r\left(a^\dagger a + \frac{1}{2}\right) + \frac{1}{2}\hbar\omega_q\sigma_z + g(a^\dagger\sigma_- + a\sigma_+), \quad (1)$$

where $\hbar$ is the reduced Planck constant, $\omega_r/2\pi = 5.668$ GHz is the resonator frequency after neon deposition, $\omega_q/2\pi$ is the qubit transition frequency, g is the electron–photon coupling strength, $a^\dagger$ and a are the photon creation and annihilation operators, respectively, and σ_z and $\sigma_\pm \equiv \sigma_x \pm i\sigma_y$ are the standard Pauli operators on a two-level system.

As an improvement from previous work, we used the high kinetic sheet inductance (~20 pH per square) of the thin TiN film to enhance the qubit–resonator coupling strength[10,29]. The trap, which is smaller than the previous device[4,5], further enhanced the MW field strength in the electron-trapping area. The estimated equivalent lumped element impedance for the differential mode was $Z_r \approx 600\ \Omega$ (Supplementary Information Section 1), which is approximately ten times that of the previous niobium (Nb) device[4]. As $g \propto \omega_r\sqrt{Z_r}$, we expected the high-impedance resonator to reach a coupling strength $g/2\pi \approx 10$ MHz (ref. 29). For high-impedance resonators, the parasitic capacitance of d.c. gates surrounding the trapping area can be comparable to the resonator capacitance[30], causing MW leakage. To minimize that, all gates were equipped with on-chip low-pass filters with an ~0.5-GHz cutoff frequency to provide over 60 dB attenuation at the resonator frequency. With this design, the resonator maintained a narrow linewidth $\kappa/2\pi$ of 0.38 MHz (Supplementary Information Section 1).

A thin layer of neon was grown on the device surface, which led to less than a 1-MHz redshift of the resonator frequency. Electrons generated from a tungsten filament were bound to this layer (Methods). At the trap, eNe qubits that strongly couple with the resonator exhibited vacuum Rabi splitting when the qubit frequencies were tuned across the resonator with the d.c. electrode. As shown in Fig. 2a, for one of the three qubits we characterized, labelled as Q1, the coupling strength extracted from the splitting gives $g/2\pi = 6.43$ MHz. Compared with the previous Nb resonator[4,5], the higher impedance of the TiN resonator enhanced the qubit–resonator coupling strength, with a maximum observed $g/2\pi$ of ~16 MHz. (See Supplementary Information Sections 2 to 5 for a detailed characterization of the three qubits Q1, Q2 and Q3.)

Noise sensitivity

We used eNe qubits as sensitive probes to characterize the environmental charge noise. Their sensitivity depends on the qubit spectral property, which can be mapped via two-tone measurements while varying the d.c. gate voltages, as shown in Fig. 2b for Q1. The extracted qubit frequency follows a hyperbolic dependence on V_{res} applied to the resonator with a charge sweet spot at 5.065 GHz (Supplementary Information Section 3). We approximated the transition frequency of the eNe qubit with a general model, which captured the measured spectroscopic features of the qubit:

$$\hbar\omega_q = \sqrt{\hbar^2(\omega_{ss} + \delta\omega_{ss})^2 + (\epsilon + \delta\epsilon + 2d_e(\mathcal{E} + \delta\mathcal{E}))^2}, \quad (2)$$

where ω_{ss} represents the charge sweet spot frequency, and ϵ describes the energy offset defining the corresponding bias voltage. The electrical tunability of the qubit transition frequency is described by the term $2d_e\mathcal{E}$, where d_e is the electron dipole moment and $\mathcal{E} \propto \Delta V_{res}$ is the applied field[31,32]. Moreover, the noise terms $\delta\mathcal{E}$, $\delta\epsilon$ and $\delta\omega_{ss}$ caused by the d.c. bias or adjacent charge fluctuations lead to decoherence of the qubit. The sensitivity of the qubit frequency ($f_q = \omega_q/2\pi$) to voltage fluctuations on the resonator electrodes can then be extracted as the frequency lever-arm $|\partial f_q/\partial V_{res}|$.

When the qubit is biased at the charge sweet spot, $|\partial f_q/\partial V_{res}| = 0$, it is first-order insensitive to voltage (charge) noise. Figure 2c,d shows that the measured total dephasing (Ramsey) time T_2^* and the total decoherence time with a Hahn echo T_2^{echo} were 8.2 μs and 21.6 μs, respectively. That T_2^{echo} approaches twice the relaxation time T_1 indicates that the low-frequency (quasi-static) noise is the dominant dephasing factor for Q1 at its charge sweet spot[33]. To reveal the high-frequency (non-static) noise distribution, we biased the qubit away from its charge sweet spot. The frequency lever-arms at the bias points used in the following noise analysis are $|\partial f_q/\partial V_{res}| = 90.2$ MHz mV^{-1}, 130.0 MHz mV^{-1}, 157.3 MHz mV^{-1} and 184.7 MHz mV^{-1}.

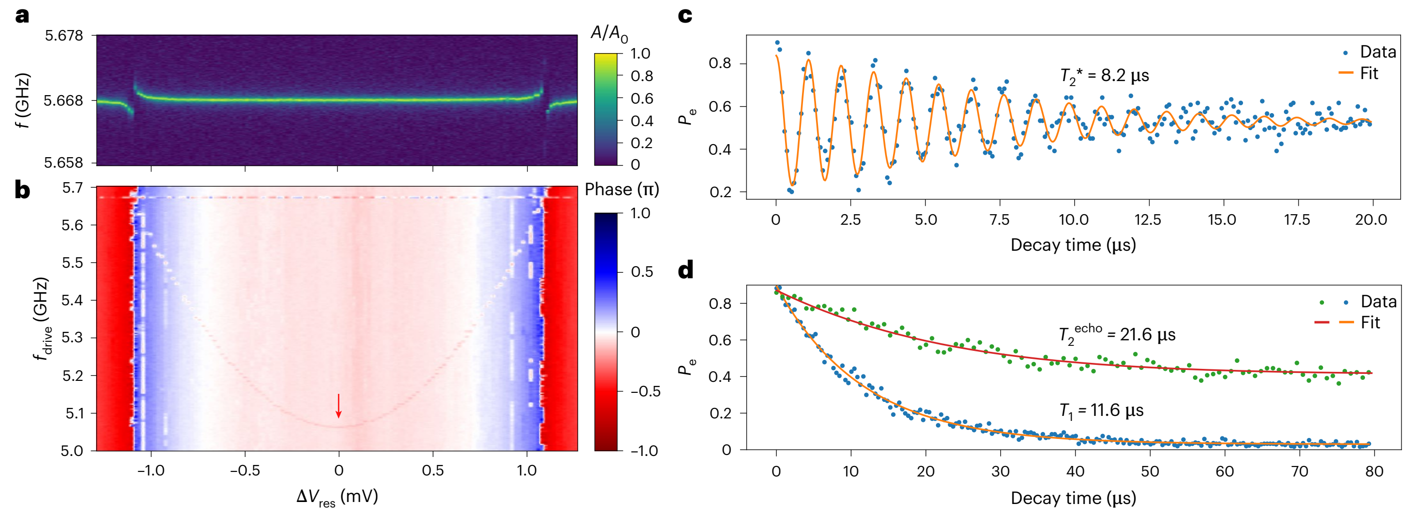

Fig. 2 | Spectroscopic and coherence properties of an eNe charge qubit Q1. **a**, Normalized MW transmission amplitude (A/A_0) centred around the resonator frequency versus the relative resonator bias voltage ΔV_{res}, as described in **b**. A_0 is the bare-resonator transmission amplitude at resonance. Two avoided crossings appear when the eNe qubit comes into resonance with the resonator. **b**, Two-tone qubit spectroscopy measurement displaying the transmission phase response at the resonator frequency ω_r versus ΔV_{res}, while weak drive tones are concurrently sent in at a frequency f_{drive}. **c**, Ramsey fringes at the charge sweet spot, marked with the red arrow in **b**. The fitted total dephasing (Ramsey) time $T_2^* = 8.2$ μs. P_e is the excited-state population of the qubit. **d**, Relaxation and Hahn echo measurements showing that the total decoherence time with a Hahn echo $T_2^{echo} = 21.6$ μs and relaxation time $T_1 = 11.6$ μs at the charge sweet spot.

Additionally, the sensitivity to gate voltage fluctuations varies between qubits (Supplementary Information Section 2). As illustrated in Fig. 1c, the local neon profile and the trap structure define the potential energy landscape seen by the electrons. Recent theoretical work has emphasized the important role of neon morphology in defining the Hamiltonian of the qubit[34,35]. The observed variations in qubit sensitivity to d.c. biases and their sweet-spot frequencies confirm the non-uniformity in the local electron-trapping potential.

Noise spectroscopy

Fluctuations in the charge environment can cause stochastic frequency shifts of the eNe qubit, which lead to qubit dephasing. As illustrated in Fig. 3a, because of the increase of the qubit sensitivity to voltage fluctuations, T_2^* for Q1 decreased to 1.93 μs when biased at $|\partial f_q/\partial V_{res}| = 184.7$ MHz mV^{-1}, corresponding to 15.9 MHz detuning from the charge sweet spot. Further, a single refocusing pulse, that is a Hahn echo, was insufficient to make the coherence time approach the relaxation limit, indicating considerable high-frequency noise components.

To probe the high-frequency components of the environmental noise on solid neon, we drove the qubit with Carr–Purcell–Meiboom–Gill (CPMG) sequences. Qualitatively, the decoherence time under CPMG sequences T_2^{CPMG} at all the bias points increased with the refocusing number N, approaching $2T_1$, as shown in Fig. 3a. The extracted pure dephasing time T_ϕ in Fig. 3b reflects the frequency-dependent noise power distribution. For a noise spectrum following $S(f) \propto 1/f^{\alpha}$, T_ϕ scales with N^{β}, where $\beta = \alpha/(1+\alpha)$ (refs. 12,13,19,36). The β fitted via this scaling relation provides a more accurate noise distribution compared with individual fittings of the decay curve according to qubit dephasing χ_N at time τ, where $\chi_N(\tau) = (\tau/T_\phi)^{\alpha+1}$ (ref. 36). For Q1, the average fitting gives $\beta = 0.6(1)$, corresponding to $\alpha = 1.5(6)$.

The CPMG sequences act as filter windows in the frequency domain. They are used to probe the noise spectral distribution[33]. For Q1, the sensing range spans from 0.01 MHz to 1 MHz, shown as the extracted total noise density in Fig. 4a. (See Methods for details of the CPMG sequence and noise calculation.) Figure 4b shows the converted voltage (charge) noise on the resonator electrode S_v, ranging from 10^{-4} μV^2 Hz^{-1} to 10^{-6} μV^2 Hz^{-1}, with a power-law fit $S_v \propto 1/f^{1.3(3)}$. A separate measurement of Q2 gave a similar voltage noise density with $S_v \propto 1/f^{1.1(3)}$ (Supplementary Information Section 4). The drop in coherence and the spectral noise distribution observed away from the sweet spot indicate that charge noise dominates the total noise when the qubit is sensitive to electrical fluctuations.

To benchmark the environmental charge noise experienced by electron qubits, Table 1 compares the converted voltage noise on adjacent gate electrodes, located ~100 nm from the qubits, across various platforms. The analysis focuses on the voltage noise spectrum from 0.01 MHz to 1 MHz, obtained from characterizations of the eNe charge qubits in this work and state-of-the-art noise records for silicon metal-oxide-semiconductor (Si-MOS), group IV heterostructures and group III–V heterostructures. The high-frequency voltage noise (between 0.01 MHz and 1 MHz) measured at the vacuum/neon interface ranges between 10^{-4} μV^2 Hz^{-1} and 10^{-6} μV^2 Hz^{-1}. This voltage noise is at least one order of magnitude lower than in some engineered semiconductor platforms[11,12,17–21,24,26] and comparable to others[13,14,25]. This result also approaches some of the best noise data (10^{-6} μV^2 Hz^{-1} to 10^{-7} μV^2 Hz^{-1} in the same frequency range) that have ever been achieved with GaAs/AlGaAs semiconductor platforms[15,16]. Based on the upper bound of the electrochemical potential lever-arm against a nearby gate (1 eV V^{-1}), the estimated charge noise (10^{-8} eV Hz$^{-1/2}$ to 10^{-9} eV Hz$^{-1/2}$ between 0.01 MHz and 1 MHz) is also comparable to the best records achieved with semiconductor qubits[13,20,25,37,38].

Among the semiconductor spin qubits used for comparison, GaAs/AlGaAs systems hold the record for the lowest voltage noise[15,16]. This characteristic may be attributed to the high-quality material growth with nearly perfect lattice matching and extremely low disorder[2]. Nonetheless, the coherence of GaAs/AlGaAs qubits is practically limited by relaxation processes stemming from strong piezoelectric electron–phonon coupling for charge qubits[39] and by nuclear spins for spin qubits[40], so that GaAs/AlGaAs is not a realistic contender for either charge or spin qubits.

For qubits based on Si-MOS or group IV materials, the origins of the dephasing charge noise are complicated. As summarized in Table 1, these include fluctuators in the bulk material as well as device- and fabrication-dependent interfaces[37,38]. In Si/SiO_2 systems, the extreme proximity of the qubit to the oxide interface and electrical gates can introduce notable disorder and noise[18,37]. In Si/SiGe and Ge/SiGe systems, amorphous gate oxides are known to host a considerable variety of two-level fluctuators[13,25,38]. Mitigating these noise sources in

https://doi.org/10.1038/s41928-026-01613-4

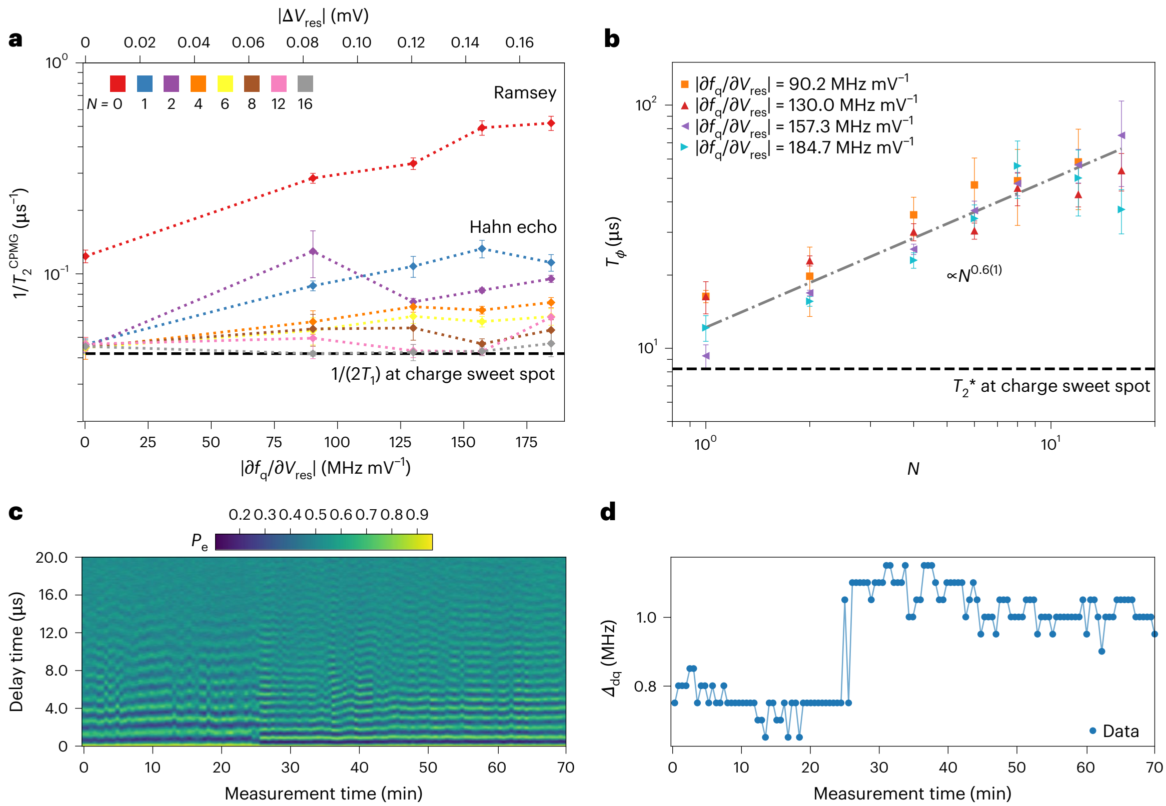

Fig. 3 | Decoherence of eNe qubit Q1. a, Extracted total decoherence rate under CPMG sequences $1/T_2^{\mathrm{CPMG}}$ from experiments. Qubit 1 (Q1) is biased at various frequency lever-arms $|\partial f_q/\partial V_{\mathrm{res}}|$. The refocusing pulse numbers $N = 0, 1, 2, 4, 6, 8, 12$ and 16, as denoted by different colours. With an increase of N, the $1/T_2^{\mathrm{CPMG}}$ of the qubit biased near the charge sweet spot approaches the limit $2T_1$. **b**, The pure dephasing time T_ϕ increases as a function of N when the qubit is biased away from charge sweet spot. The power-law fit gives $T_\phi \propto N^{0.6(1)}$. **c**, Repeated Ramsey fringes measured near the qubit sweet spot for 128 iterations. Each recording took 33 s. **d**, Detuning Δ_{dq} between the drive tone and the qubit frequency during the Ramsey measurements, which reveals stochastic frequency shifts. All error bars represent one standard error for the extracted parameters (Methods).

semiconductor platforms often requires intricate material engineering and interface optimization.

The charge noise for the present eNe charge qubits is probably not intrinsic to the solid neon material but due to the excess electrons trapped on the rough neon surface[34,35] and the surface fluctuators from device substrates. Improving the film smoothness and thickness and refining the electron-loading procedure could mitigate these dominant extrinsic noise sources. Despite the current imperfect implementation, the above noise analysis is consistent with the coherence of the eNe charge qubits being orders of magnitude longer than reported for semiconductor charge qubits[41]. These results not only show that solid neon can serve as a low-noise environment for electron charge qubits but they also predict a long coherence time for electron spin qubits in this system (Supplementary Information Section 6).

In addition to the high-frequency range, we also investigated the low-frequency noise at the charge sweet spot. Figure 3c,d shows variations in the frequency for Q1 revealed by Ramsey measurements[12,13] that were repeated for ~1 h after Q1 was initially biased near its charge sweet spot. The qubit underwent a discrete frequency transition with various magnitudes, as seen near the 25-min point of the 1-h trace. This was revealed by a fast Fourier transform of the Ramsey signals (Methods and Supplementary Information Section 3). Using a periodogram method, we converted this 1-h qubit frequency measurement into a frequency noise spectrum over 10^{-3} Hz to 10^{-1} Hz, as shown in Fig. 4a. A power-law fit of the data gives the relation $S \propto f^{-1.1(2)}$. Other detection methods, such as single-electron charge sensing techniques[13], could complete the noise spectrum in the middle-frequency range from 1 Hz to 10^4 Hz.

Although the qubit is first-order insensitive to small charge (voltage) fluctuations at the sweet spot, its local trapping potential remains vulnerable to low-frequency perturbations from second-order effects. These are probably caused by the rearrangement of excess electrons trapped on the rough neon surface, which are difficult to remove because of their low mobility. Growing smoother neon films and employing gate-controlled electron-loading schemes[42] may help to mitigate these low-frequency fluctuations.

To complete the discussion, we calculated the transverse noise at the qubit frequencies contributing to energy relaxation with $1/T_1 = \pi/2 \times S(2\pi f_q)$ (ref. 33). In Fig. 2d, the measured $T_1 = 11.6$ μs at the charge sweet spot of Q1, where the Purcell rate of Q1 to the resonator mode is $\Gamma_r = \kappa g^2/\Delta_{\mathrm{rq}}^2 = 1/3.9\ \mathrm{ms}^{-1}$. Δ_{rq} is the detuning between the resonator and the qubit, and κ is the resonator decay rate. Unlike the qubits reported in our previous work[5], this result indicates that non-radiative decay channels dominate the energy relaxation of Q1, as is the case for the other two qubits as well. Relaxation via phonon emission[7,28,43] and interaction with excess surface electrons, which can act as a background bath of two-level systems[44], may limit the relaxation lifetime of floating electron qubits. Measurements of T_1 of Q1 at various bias frequencies showed that the transverse noise increases with frequency in the gigahertz range, probably due to the interaction with an ohmic-type environment[1]. The best fit of the total transverse noise versus frequency in a log scale gives $S \propto f^{2.2(2)}$ between 5.065 GHz and 5.498 GHz, with a mean of $3.6 \times 10^5\ \mathrm{Hz^2\ Hz^{-1}}$, as shown in Fig. 4c.

Temperature dependence

To characterize the robustness of the solid neon film as an electron qubit host at elevated temperatures, we measured the temperature dependence of the relaxation of Q1 and its coherence at its charge sweet spot from 10 mK to 500 mK. The energy relaxation T_1 is described well by a

https://doi.org/10.1038/s41928-026-01613-4

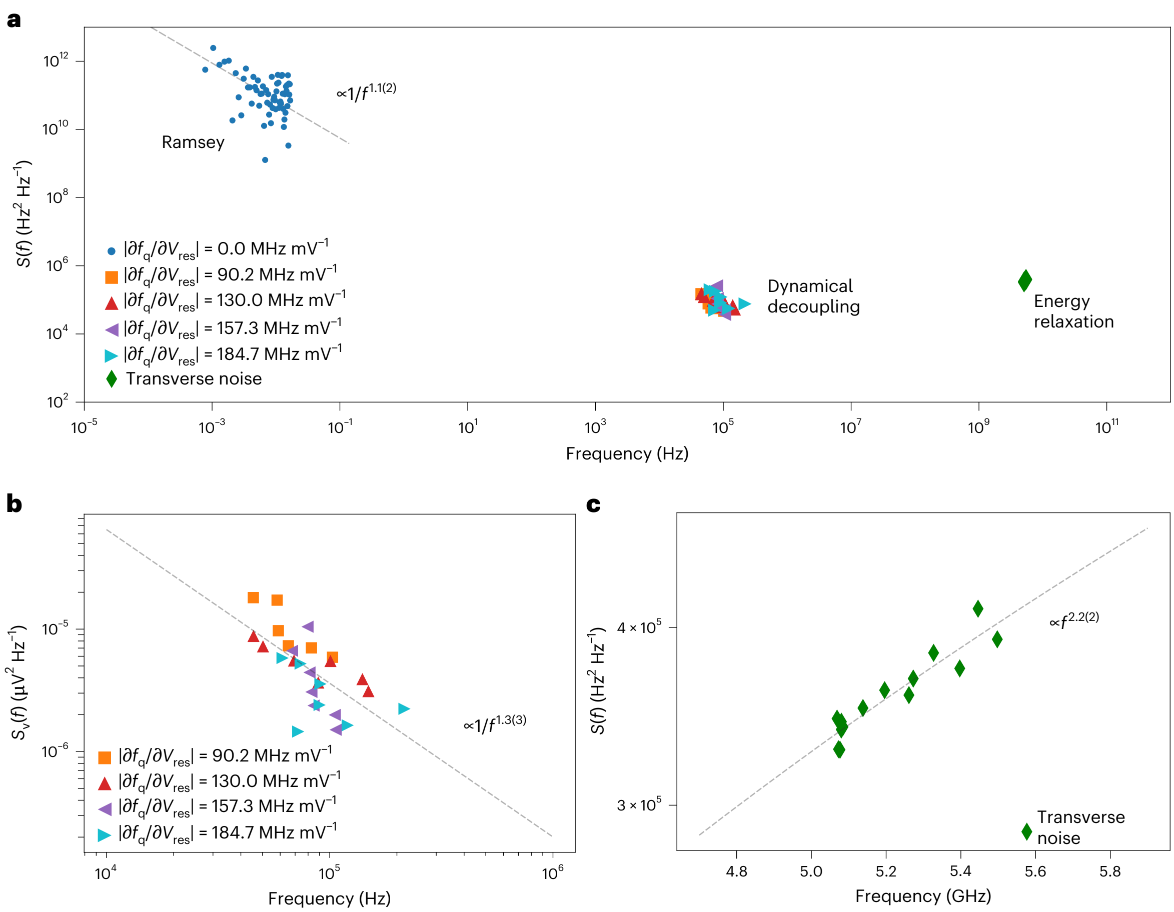

Fig. 4 | Noise spectroscopy of eNe qubit Q1. a, Data between 0.01 MHz and 1 MHz are the total longitudinal noise density (coloured dots) derived from dynamical decoupling data at different qubit bias points. Data between 10^{-3} Hz and 10^{-1} Hz are the extracted total longitudinal noise (blue dots) from long-term Ramsey measurements when biased at the charge sweet spot. Data near 5.0 GHz are the transverse noise of the eNe qubit (green diamonds). *S*(*f*) represents the noise spectral density with *f* denoting the frequency. **b**, Voltage noise density $S_V(f)$ between 0.01 MHz and 1 MHz, projected on the resonator electrode. **c**, Zoom-in of the transverse noise in **a** between 5.0 GHz and 5.6 GHz. Notice that the *x* axis is linear with a unit of gigahertz. Grey dashed lines are power-law fits of the frequency-dependent noise.

model that accounts only for the coupling of a two-level quantum system to a bosonic thermal bath within the experimental temperature range, $T_1 \propto \tanh(\hbar\omega_q/2k_BT)$ (refs. 45,46), as shown in Fig. 5a. Here $\hbar$ is the reduced Planck constant, k_B is the Boltzmann constant and T is temperature. Similarly, the thermal population follows a Maxwell–Boltzmann distribution[47] (Supplementary Information Section 3). The corresponding electron temperature closely tracks the mixing chamber (MXC) temperature between 100 mK and 500 mK and saturates around 40 mK, demonstrating the effective cooling of electrons at low temperatures.

A separate measurement on a different qubit, Q2, as presented in Supplementary Information Section 4, revealed a similar temperature dependence for T_1 but with a different low-temperature limit. This indicates a picture in which individual eNe qubits couple differently to their environment (including through phonons[7,28]), which sets the low-temperature T_1. This motivates further studies of the microscopic limitations of T_1. For the current qubits with transition frequencies near 5 GHz, T_1 decreased to about half of its low-temperature value at 200 mK. Given the temperature-dependent T_1 scaling with the two-level quantum system model, we anticipate further improvements to the high-temperature performance of eNe qubits from engineering charge or spin states for qubit operations at higher frequencies. This would motivate the development of dedicated circuit quantum electrodynamics architectures and control hardware, for which recent efforts have already begun in superconducting qubits operating above 20 GHz (ref. 22).

The coherence data at elevated temperatures (Fig. 5b) show the thermal robustness of solid neon as an electron qubit host. Q1, with a qubit frequency of only ~5 GHz, maintained T_2^{echo} temperatures of up to 400 mK for >1 μs, indicating the potential of eNe for high-temperature operations. Moreover, the trend for coherence with temperature remains complex. T_2^* and T_2^{echo} show that quasi-static and high-frequency noise components behave differently with increased temperature, as shown in Fig. 5b. Below 50 mK, T_2^{echo} approaches $2T_1$, indicating a weak noise density in the high-frequency range. However, starting from 75 mK, T_2^{echo} scales with temperature proportional to $T^{-1.1(1)}$ and quickly degrades from $2T_1$, indicating the rise of non-quasi-static dephasing noises at higher temperatures[15]. On the other hand, $T_2^* \propto T^{-0.72(4)}$ in the whole testing range.

The extracted pure dephasing time T_ϕ indicates that the decoherence of the qubit due to non-quasi-static noise grew primarily due to thermal effects at elevated temperatures. As shown in Fig. 5c, T_ϕ began to decrease notably when the MXC temperature exceeded 100 mK. In this range, the measured data match well with a parameter-free model that accounts for the effect of resonator thermal photons on the qubit dephasing[22]:

$$T_\phi^{-1} = \frac{\kappa}{2}\mathrm{Re}\left[\sqrt{\left(1+\frac{2i\chi}{\kappa}\right)^2 + \frac{8i\chi}{\kappa}n_{th}} - 1\right], \quad (3)$$

where χ is the dispersive shift for the resonator (Supplementary Information Section 3). n_{th} represents the resonator thermal photon

Table 1 | Comparison of voltage noise and prospective noise origins for electron (hole) qubits on solid neon and in various semiconductor platforms

Qubit platform	Host interface	Voltage noise S_v ($\mu V^2 Hz^{-1}$) at 0.01–1 MHz	Reference	Prospective sources of charge dephasing noise
eNe	Vacuum/neon	10^{-4}–10^{-6}	This work	Excess electrons on neon; Substrate surfaces under neon; refs. 34,35
Si-MOS	Si/SiO$_2$	10^{0}–10^{-2}	12	Surfaces and interfaces of electrical gates; Si/SiO$_2$ interface; SiO$_2$ layer; refs. 18,37
	Si/SiO$_2$	10^{-1}–10^{-3}	17	
	^{28}Si/^{28}SiO$_2$	10^{-1}–10^{-3}	18	
Group IV heterostructures	Si/SiGe	10^{-3}–10^{-5}	13	Amorphous gate oxide; Strained heterostructure interfaces; In quantum wells confining the electrons; refs. 13,25,38
	Si/SiGe	10^{-1}–10^{-3}	21	
	^{28}Si/SiGe	10^{-2}–10^{-4}	11	
	^{28}Si/SiGe	10^{-2}–10^{-4}	19	
	^{28}Si/SiGe	10^{-1}–10^{-3}	20	
	Ge/SiGe	10^{-1}–10^{-3}	24	
	Ge/SiGe	10^{-3}–10^{-5}	25	
	Ge/SiGe	10^{-1}–10^{-3}	26	
Group III–V heterostructures	GaAs/AlGaAs	10^{-3}–10^{-5}	14	Carrier traps in the heterostructure Gate leakage; refs. 59–61
	GaAs/AlGaAs	10^{-6}–10^{-7}	15,16	

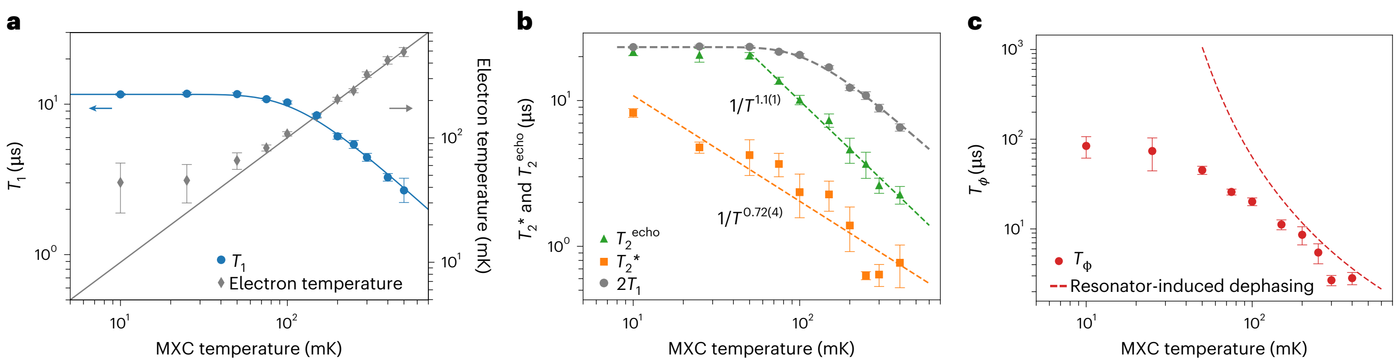

Fig. 5 | Temperature-dependent coherence of eNe qubit Q1 at the charge sweet spot. a, Relaxation time T_1 (blue dots, data) versus MXC temperature. The solid curve represents the predicted $T_1(T) = T_1(T=0)\tanh(\hbar\omega_q/2k_BT)$. We used the value measured at 10 mK for $T_1(T=0)$ and the MXC temperature as T. What is also shown is the extracted electron temperature (grey diamonds, data) versus the MXC temperature based on the measured thermal population in Supplementary Information Section 3. **b**, Decoherence time T_2^* (orange squares) and T_2^{echo} (green triangles) versus the MXC temperature with a fitted power law (dashed curves). Grey dots and curves show $2T_1$ for comparison. **c**, Extracted pure dephasing time T_ϕ as a function of the MXC temperature. The red dashed curve is the parameter-free calculation of the resonator-induced dephasing based on Q1 properties. All error bars represent one standard error for the extracted parameters (Methods).

population, equal to $1/(e^{hf_r/k_BT}-1)$, with f_r the resonator frequency. Nevertheless, the deviation of the data from the model below 100 mK indicates the presence of other low-temperature dephasing mechanisms. Separate measurements on Q2 (Supplementary Information Section 4) gave similar results. Using higher frequency resonators[22] could help to suppress the photon-noise-induced dephasing.

Conclusions

We have reported a quantitative investigation of the environmental noise isolation provided by a thin neon layer for eNe qubits. We have shown that eNe qubits are resilient to temperature and could be used for high-temperature operations. Improving the consistency of the system in terms of qubit properties and noise isolation will be an important next step in the development of eNe qubits. Our work also highlights the importance of improving neon growth and electron-generating and electron-trapping techniques.

The various spectral properties of eNe qubits indicate that the local neon profile is crucial in electron-trapping mechanisms. The surface roughness of cryogenic solid neon and hydrogen films has been studied using optical methods and surface electron mobility measurements[48]. With the current set-up and neon-filling approach, the cryogenic adsorption of neon back into the 4K section of the fill lines during the cooldown and the triple-point (de)wetting[48] may result in a large surface roughness on the thin neon films. The morphology of the underlying substrate could also translate to the neon surface and affect the properties of trapped eNe qubits[35]. Developing a neon growth method with more refined control—including cryogenic valve[49] and temperature regulation and repetitive annealing[50]—as well as exploring condensation methods[51] could improve neon film quality and qubit uniformity. Additionally, the position of trapped electrons relative to the nearby electrodes determines the frequency lever-arm and the sensitivity of the qubit to voltage fluctuations. At present, the lack of a precise method for growing solid neon makes the electron trapping uncertain, which induces variations in the qubit properties.

Improving the consistency and control over individual eNe qubits is also important for scaling up. All-MW and fast d.c. types of two-qubit gates could be applied to eNe qubits coupled through a resonator bus[52] or direct charge–charge interactions[53]. They all require stable and efficient control over qubit properties. In both regards, refined neon growth methods, gated electron-loading mechanisms and electron detectors with higher spatial resolution should be developed.

However, the diverse noise behaviour observed in eNe qubits reflects the complexity of the local charge environment. We have shown that for two eNe qubits, a single refocusing pulse is insufficient to mitigate most of the noise at the sweet spots of the qubits, indicating a higher noise density in the high-frequency range (Supplementary Information Sections 4 and 5). The different spectral noise distributions indicate locally non-uniform noise sources, as the coherence of a qubit is highly sensitive to the density and distribution of fluctuators[54]. Excess electrons emitted by the tungsten filament could result in non-uniformly distributed charge fluctuators on the neon surface. A rearrangement of excess charges adjacent to the qubit may contribute to the low-frequency qubit drift and occasional electron escape events[55]. Fluctuations of distant charges may also perturb the qubits via the high-impedance resonator due to the enhanced coupling strength. The thinness of the neon film could have further reduced the effectiveness of isolating noise embedded in the underlying substrate. Strategies for improving the coherence of the qubit include developing electron-loading procedures on thicker films (~100 nm)[10,42] and separating trapped qubits from adjacent charge reservoirs[56] with protection gates.

Finally, the limiting factor for the non-radiative energy relaxation rate of eNe qubits needs further investigation. The non-monotonic variations in T_1 for qubits with different charge sweet spot frequencies point to variations in the non-radiative decay channels. Nearby charges may create a sparse bath of two-level fluctuators weakly coupled to the eNe qubit, whose density determines the transverse noise intensity[54]. Electrical gating could be applied to bias or repel those weakly coupled charges to reduce the relaxation rate[57]. In addition, the rough neon surface may create more channels for phonon-induced relaxation, compared with electrons on flat neon or helium, due to symmetry breaking for otherwise forbidden selection rule processes[7,43]. With the development of improved electron-generating and electron-trapping methods on thicker and smoother neon, we anticipate improvements in both the coherence and long-term stability of eNe qubits.

Methods

Device and set-up

The resonator, electrode and on-chip filter were patterned with electron beam lithography followed by reactive-ion etching. Around the traps, the Si substrate was etched down by ~250 nm to host the thin neon layer. Unlike the previous device, which was originally designed to trap electrons on helium[4,5] so that the resonator was embedded in a 1-µm-deep channel to host liquid helium, the TiN resonator in our device was positioned at the same level as the ground plane[35]. Moreover, the two-trap design had the broader goal of coupling two distant eNe qubits via the resonator bus[52]. See details of the characterization of the TiN film, resonator and on-chip filter in Supplementary Information Section 1.

The experimental set-up was like that described in our previous works[4,5]. The chip was mounted on a customized printed circuit board within a vacuum-sealed copper cell, which provided d.c. and MW interfaces. A gas filling line was attached to the top lid of the cell and used to deposit neon at cryogenic temperatures. A tungsten filament was used as the electron source. The cell was mounted on the MXC plate of a dilution refrigerator. A total attenuation of 60 dB was applied on the cryogenic segment of the MW input line with infrared filters (QMC-CRYOIRF-004). The MW output line was equipped with cryogenic isolators (LNF-ISISC4_12A) at the MXC plate, which was followed by a high-electron-mobility transistor amplifier (LNF-LNC4_8C) at the 4K plate and room-temperature amplification. All d.c. connections were filtered with thermocoax cables, inductor–capacitor (LC) filters (Mini-Circuits RLP-30+) and home-made low-pass filters with a 150-Hz cutoff. Qubit spectroscopic measurements were conducted with a vector network analyser (Keysight N5222B) and a signal generator (Anritsu MG3692C). Time-domain pulse measurements were conducted with Quantum Machine OPX+ and Octave. The d.c. gates were applied with QDevil QDAC-II.

Neon growth

The neon filling used the following procedure. The fridge was warmed up from its base temperature with a heater mounted on the 4K plate. At that point, the helium mixture circulation was turned off and all the mixture was collected while the pulse tube was still on. The heater power was set so that it created a temperature gradient from 27 K at the 4K plate to about 25 K at the MXC plate. Under these conditions, the neon gas was filled into the apparatus and deposited onto the device chip in its liquid phase. After filling, the heater was turned off, and the whole fridge was cooled down again to let the liquid neon freeze into a solid. During the cooldown, we annealed the neon film at 10 K for 1 h.

Electron deposition

Electrons were ejected from the tungsten filament mounted on the lid of the hermetic copper cell. When the dilution fridge had cooled down to the base temperature, the total resistance on the filament loop was 2 Ω. A current pulse train applied by a pulse generator with a voltage output of −0.6 V, pulse width of 0.1 ms, repetition frequency of 1 kHz and duration of 0.3 s was used to fire electrons. We noticed that applying a higher voltage or longer duration caused too many electrons to land on the top of the chip, which reduced the stability of the trapped electrons. Only when both the neon film was present on the sample surface and electrons were emitted did we see signatures of trapped eNe qubits strongly coupled to the resonator (Supplementary Information Section 7).

Noise characterization

We used the dynamical decoupling technique with CPMG pulse sequences to study the spectral distribution of the high-frequency noise affecting the eNe qubits[33]. All qubit bias points had positive ΔV_{res}. In the sequence, N refocusing Y_π pulses were applied between two $X_{\pi/2}$ pulses with identical separation τ/N between two pulses. Under such sequences, the qubit coherence decayed following $P_{\mathrm{e}}(N,\tau) = P_0 + a\,\exp(-\tau/2T_1)\,\exp(-\chi_{\mathrm{P}})\,\exp(-\chi_N(\tau))$, with terms accounting for pure dephasing $-\chi_N$, energy relaxation $-\tau/2T_1$ and decay during driving pulses $-\chi_{\mathrm{P}}$ (ref. 33). P_0 is the constant corresponding to the qubit population when τ approaches ∞, while P_0+a corresponds to the qubit population when τ equals 0. We define T_2^{CPMG} as the time when the coherence of the qubit had decayed by a factor 1/e due to energy relaxation and pure dephasing. Increasing the number of Y_π pulses reduced the time the qubit was exposed to noise before each refocusing, thereby extending the coherence time. Under the assumption of Gaussian noise[33], a CPMG sequence with N refocusing pulses and total delay time of τ imposed a filter function $g_N(\omega,\tau)$ to the qubit noise caused by source λ with spectral distribution $S_\lambda(\omega)$, which determined the qubit dephasing $\chi_N(\tau)$:

$$\chi_N(\tau) = \tau^2 \sum_\lambda \left(\frac{\partial\omega_{\mathrm{q}}}{\partial\lambda}\right)^2 \int_0^\infty S_\lambda(\omega) g_N(\omega,\tau)\,\mathrm{d}\omega, \tag{4}$$

where $\partial\omega_{\mathrm{q}}/\partial\lambda$ is the sensitivity of the qubit transition frequency to noise source λ, the filter function $g_N(\omega,\tau) = |y_N(\omega,\tau)|^2/(\omega\tau)^2$ and $y_N(\omega,\tau) = 1 + (-1)^{1+N}\exp(i\omega\tau) + 2\sum_{j=1}^{N}(-1)^j \exp(i\omega\tau(j-0.5)/N)\cos(\omega\tau_\pi/2)$.

With the noise filter imposed by the CPMG sequence, we approximated the total noise power spectrum density S at frequency f_N as (refs. 12,13):

$$S(2\pi f_N) = \frac{1}{(T_\phi)^2 g_N(2\pi f_N, T_\phi)\Delta\omega_N}, \tag{5}$$

where $2\pi f_N$ is the peak angular frequency of the first harmonic of $g_N(\omega, T_\phi)$, and $\Delta\omega_N$ is the full-width at half-maximum of the peak. T_ϕ is the time when $\chi_N(T_\phi) = 1$. Given the qubit sensitivity $|\partial f_{\mathrm{q}}/\partial V_{\mathrm{res}}|$, as listed in the legends of Figs. 3 and 4, and neglecting other potential noise sources, we extracted the equivalent voltage noise (S_{v}):

$$S(2\pi f) = (\partial f_{\mathrm{q}}/\partial V_{\mathrm{res}})^2 \times S_{\mathrm{v}}(2\pi f). \tag{6}$$

To investigate the low-frequency dynamics of qubit decoherence near the charge sweet spot, we repeatedly conducted Ramsey measurements for 128 iterations, with each recording taking 33 s (refs. 12,13). As shown in Fig. 3d, we extracted the qubit frequency drift through a fast Fourier transform analysis of the measured Ramsey fringes. During the measurement, we also observed more drastic qubit frequency fluctuations on the scale of 10–100 MHz, corresponding to 0.14–0.44 mV for ΔV_{res}. Sometimes, we even observed the disappearance of qubit signatures in the usual gate scanning range. These qubit frequency 'jumps' usually occurred less than 0.5 times per hour. We attribute these large fluctuations to charge rearrangements of nearby weakly trapped electrons on neon[55]. We ensured that the qubit remained relatively stable and free from such notable fluctuations during data collection for all the presented measurements at various bias points.

For all time-domain decoherence and relaxation measurements, each data point was averaged over 500 single-shot read-outs.

Data availability

The source data of this study are available via Zenodo at https://doi.org/10.5281/zenodo.18548730 (ref. 58). Other data that support the findings are available from the corresponding authors upon request.

Code availability

The codes used for analysing and plotting the data in this work are available from the corresponding authors upon request.

References

1. Paladino, E., Galperin, Y., Falci, G. & Altshuler, B. 1/*f* noise: implications for solid-state quantum information. *Rev. Mod. Phys.* **86**, 361–418 (2014).
2. Burkard, G., Ladd, T. D., Pan, A., Nichol, J. M. & Petta, J. R. Semiconductor spin qubits. *Rev. Mod. Phys.* **95**, 025003 (2023).
3. De Leon, N. P. et al. Materials challenges and opportunities for quantum computing hardware. *Science* **372**, eabb2823 (2021).
4. Zhou, X. et al. Single electrons on solid neon as a solid-state qubit platform. *Nature* **605**, 46–50 (2022).
5. Zhou, X. et al. Electron charge qubit with 0.1 millisecond coherence time. *Nat. Phys.* **20**, 116–122 (2024).
6. Petersson, K., Petta, J., Lu, H. & Gossard, A. Quantum coherence in a one-electron semiconductor charge qubit. *Phys. Rev. Lett.* **105**, 246804 (2010).
7. Chen, Q., Martin, I., Jiang, L. & Jin, D. Electron spin coherence on a solid neon surface. *Quantum Sci. Technol.* **7**, 045016 (2022).
8. Guo, W., Konstantinov, D. & Jin, D. Quantum electronics on quantum liquids and solids. *Progress in Quantum Electron.* **99**, 100552 (2024).
9. Jennings, A., Zhou, X., Grytsenko, I. & Kawakami, E. Quantum computing using floating electrons on cryogenic substrates: potential and challenges. *Appl. Phys. Lett.* **124**, 120501 (2024).
10. Tian, Y. et al. NbTiN nanowire resonators and prospects for spin-photon coupling with electrons on solid neon. *Phys. Rev. Appl.* **25**, 024011 (2026).
11. Eng, K. et al. Isotopically enhanced triple-quantum-dot qubit. *Sci. Adv.* **1**, e1500214 (2015).
12. Jock, R. M. et al. A silicon singlet–triplet qubit driven by spin–valley coupling. *Nat. Commun.* **13**, 641 (2022).
13. Connors, E. J., Nelson, J., Edge, L. F. & Nichol, J. M. Charge-noise spectroscopy of Si/SiGe quantum dots via dynamically-decoupled exchange oscillations. *Nat. Commun.* **13**, 940 (2022).
14. Cerfontaine, P. et al. Feedback-Tuned noise-resilient gates for encoded spin qubits. Preprint at http://arxiv.org/abs/1606.01897 (2016).
15. Dial, O. et al. Charge noise spectroscopy using coherent exchange oscillations in a singlet-triplet qubit. *Phys. Rev. Lett.* **110**, 146804 (2013).
16. Cerfontaine, P. et al. Closed-loop control of a GaAs-based singlet-triplet spin qubit with 99.5% gate fidelity and low leakage. *Nat. Commun.* **11**, 4144 (2020).
17. Klemt, B. et al. Electrical manipulation of a single electron spin in CMOS using a micromagnet and spin–valley coupling. *npj Quantum Inf.* **9**, 107 (2023).
18. Zwerver, A. et al. Qubits made by advanced semiconductor manufacturing. *Nat. Electron.* **5**, 184–190 (2022).
19. Yoneda, J. et al. A quantum-dot spin qubit with coherence limited by charge noise and fidelity higher than 99.9%. *Nat. Nanotechnol.* **13**, 102–106 (2018).
20. Struck, T. et al. Low-frequency spin qubit energy splitting noise in highly purified ^{28}Si/SiGe. *npj Quantum Inf.* **6**, 40 (2020).
21. Kawakami, E. et al. Gate fidelity and coherence of an electron spin in an Si/SiGe quantum dot with micromagnet. *Proc. Natl Acad. Sci. USA* **113**, 11738–11743 (2016).
22. Anferov, A., Harvey, S. P., Wan, F., Simon, J. & Schuster, D. I. Superconducting qubits above 20 GHz operating over 200 mK. *PRX Quantum* **5**, 030347 (2024).
23. Huang, J. Y. et al. High-fidelity spin qubit operation and algorithmic initialization above 1 K. *Nature* **627**, 772–777 (2024).
24. Hendrickx, N. W. et al. A four-qubit germanium quantum processor. *Nature* **591**, 580–585 (2021).
25. Stehouwer, L. E. A. et al. Exploiting strained epitaxial germanium for scaling low-noise spin qubits at the micrometre scale. *Nat. Mater.* **24**, 1906–1912 (2025).
26. Hendrickx, N. et al. Sweet-spot operation of a germanium hole spin qubit with highly anisotropic noise sensitivity. *Nat. Mater.* **23**, 920–927 (2024).
27. Shearrow, A. et al. Atomic layer deposition of titanium nitride for quantum circuits. *Appl. Phys. Lett.* **113**, 212601 (2018).
28. Schuster, D., Fragner, A., Dykman, M., Lyon, S. & Schoelkopf, R. Proposal for manipulating and detecting spin and orbital states of trapped electrons on helium using cavity quantum electrodynamics. *Phys. Rev. Lett.* **105**, 040503 (2010).
29. Koolstra, G. et al. High-impedance resonators for strong coupling to an electron on helium. *Phys. Rev. Appl.* **23**, 024001 (2025).
30. Harvey-Collard, P. et al. On-chip microwave filters for high-impedance resonators with gate-defined quantum dots. *Phys. Rev. Appl.* **14**, 034025 (2020).
31. Hung, C.-C. et al. Probing hundreds of individual quantum defects in polycrystalline and amorphous alumina. *Phys. Rev. Appl.* **17**, 034025 (2022).
32. Hegedüs, M. et al. In situ scanning gate imaging of individual quantum two-level system defects in live superconducting circuits. *Sci. Adv.* **11**, eadt8586 (2025).
33. Bylander, J. et al. Noise spectroscopy through dynamical decoupling with a superconducting flux qubit. *Nat. Phys.* **7**, 565–570 (2011).
34. Kanai, T., Jin, D. & Guo, W. Single-electron qubits based on quantum ring states on solid neon surface. *Phys. Rev. Lett.* **132**, 250603 (2024).
35. Zheng, K., Song, X. & Murch, K. W. Surface-morphology-assisted trapping of strongly coupled electron-on-neon charge states. *Phys. Rev. Lett.* **135**, 080601 (2025).
36. Medford, J. et al. Scaling of dynamical decoupling for spin qubits. *Phys. Rev. Lett.* **108**, 086802 (2012).
37. Elsayed, A. et al. Low charge noise quantum dots with industrial CMOS manufacturing. *npj Quantum Inf.* **10**, 70 (2024).
38. Paquelet Wuetz, B. et al. Reducing charge noise in quantum dots by using thin silicon quantum wells. *Nat. Commun.* **14**, 1385 (2023).
39. Stavrou, V. & Hu, X. Charge decoherence in laterally coupled quantum dots due to electron–phonon interactions. *Phys. Rev. B* **72**, 075362 (2005).

40. Malinowski, F. K. et al. Notch filtering the nuclear environment of a spin qubit. *Nat. Nanotechnol.* **12**, 16–20 (2017).
41. Stano, P. & Loss, D. Review of performance metrics of spin qubits in gated semiconducting nanostructures. *Nat. Rev. Phys.* **4**, 672–688 (2022).
42. Koolstra, G., Yang, G. & Schuster, D. I. Coupling a single electron on superfluid helium to a superconducting resonator. *Nat. Commun.* **10**, 5323 (2019).
43. Dykman, M., Platzman, P. & Seddighrad, P. Qubits with electrons on liquid helium. *Phys. Rev. B* **67**, 155402 (2003).
44. Müller, C., Lisenfeld, J., Shnirman, A. & Poletto, S. Interacting two-level defects as sources of fluctuating high-frequency noise in superconducting circuits. *Phys. Rev. B* **92**, 035442 (2015).
45. Lisenfeld, J. et al. Measuring the temperature dependence of individual two-level systems by direct coherent control. *Phys. Rev. Lett.* **105**, 230504 (2010).
46. Leggett, A. J. et al. Dynamics of the dissipative two-state system. *Rev. Mod. Phys.* **59**, 725 (1987).
47. Jin, X. et al. Thermal and residual excited-state population in a 3D transmon qubit. *Phys. Rev. Lett.* **114**, 240501 (2015).
48. Leiderer, P. Surface electrons on solid quantum substrates: a brief review. *J. Low Temp. Phys.* **219**, 262–281 (2025).
49. Dotsenko, V. & Mulders, N. A really simple cryogenic valve. *J. Low Temp. Phys.* **134**, 443–446 (2004).
50. Matkovic, K. et al. Characterizing neon thin film growth with an NbTiN superconducting resonator array. Preprint at http://arxiv.org/abs/2510.21029 (2025).
51. Kanagin, A. N. et al. Impurities in cryogenic solids: a new platform for hybrid quantum systems. Preprint at http://arxiv.org/abs/2508.21651 (2025).
52. Majer, J. et al. Coupling superconducting qubits via a cavity bus. *Nature* **449**, 443–447 (2007).
53. Beysengulov, N. R. et al. Coulomb interaction-driven entanglement of electrons on helium. *PRX Quantum* **5**, 030324 (2024).
54. Mehmandoost, M. & Dobrovitski, V. Decoherence induced by a sparse bath of two-level fluctuators: peculiar features of 1/*f* noise in high-quality qubits. *Phys. Rev. Res.* **6**, 033175 (2024).
55. Kuhlmann, A. V. et al. Charge noise and spin noise in a semiconductor quantum device. *Nat. Phys.* **9**, 570–575 (2013).
56. Yang, C. H. et al. Operation of a silicon quantum processor unit cell above one kelvin. *Nature* **580**, 350–354 (2020).
57. Zheng, W. et al. Coherence enhancement of solid-state qubits by local manipulation of the electron spin bath. *Nat. Phys.* **18**, 1317–1323 (2022).
58. Li, X. et al. Source data for 'Solid neon as a noise-resilient host for electron qubits above 100 mK'. *Zenodo* https://doi.org/10.5281/zenodo.18548730 (2026).
59. Sakamoto, T., Nakamura, Y. & Nakamura, K. Distributions of single-carrier traps in GaAs/$Al_xGa_{1-x}As$ heterostructures. *Appl. Phys. Lett.* **67**, 2220–2222 (1995).
60. Buizert, C. et al. In situ reduction of charge noise in GaAs/$Al_xGa_{1-x}As$ Schottky-gated devices. *Phys. Rev. Lett.* **101**, 226603 (2008).
61. Bermeister, A., Keith, D. & Culcer, D. Charge noise, spin–orbit coupling, and dephasing of single-spin qubits. *Appl. Phys. Lett.* **105**, 192102 (2014).

Acknowledgements

D.J., X.H. and X.L. acknowledge support from the Directed Research and Development programme at Argonne National Laboratory for experimental set-ups. D.J., X.L. and Y.W. acknowledge support from the Air Force Office of Scientific Research (Award No. FA9550-23-1-0636 for device fabrication and simulation). D.J. acknowledges support from the Department of Energy (DOE) (Award No. DE-SC0025542 for material growth and characterization). D.J. and W.G. acknowledge support from the National Science Foundation (NSF) (Award No. OSI-2426768 for theoretical modelling). D.J., X. Zhou and Y.H. acknowledge support from the Julian Schwinger Foundation for Physics Research for instrument development. B.D. acknowledges support from the NSF (Award No. DMR-1906003). C.S.W. and X.L. acknowledge support from Q-NEXT, one of the US DOE Office of Science National Quantum Information Science Research Centers. W.G. acknowledges support from the Gordon and Betty Moore Foundation (Grant DOI 10.37807/gbmf11567) and the National High Magnetic Field Laboratory at Florida State University, which is supported by the NSF (Cooperative Agreement No. DMR-2128556) and the state of Florida. X. Zhang and Y.H. acknowledge support from the Young Investigator Program of the Office of Naval Research (Award No. N00014-23-1-2144). X.H. acknowledges support from the France and Chicago Collaborating in the Sciences programme. Work performed at the Center for Nanoscale Materials, a US DOE Office of Science User Facility, was supported by the US DOE, Office of Basic Energy Sciences (Contract No. DEAC02-06CH11357). We thank X. Hu, R. Joynt, D. I. Schuster and A. Yacoby for helpful discussions.

Author contributions

X.L., X. Zhou and D.J. devised the experiments. X.H. and D.J. advised on the experiments. X.L. and C.S.W. conducted the experiments. X.L. designed and fabricated the device. X.L., C.S.W. and B.D. analysed the data. Y.H., X. Zhang and X.H. supported the experimental measurements. Y.W. and W.G. supported the theoretical calculations. D.J. conceived the idea and led the project. X.L., C.S.W., X. Zhou and D.J. wrote the original paper. All authors contributed to the work.

Competing interests

The authors declare no competing interests.

Additional information

Supplementary information The online version contains supplementary material available at https://doi.org/10.1038/s41928-026-01613-4.

Correspondence and requests for materials should be addressed to Xu Han, Xianjing Zhou or Dafei Jin.

Peer review information *Nature Electronics* thanks Maja Cassidy and the other, anonymous, reviewer(s) for their contribution to the peer review of this work.